PHYSICAL REVIEW E **87**, 063002 (2013)

Spatiotemporal evolution of hairpin eddies, Reynolds stress, and polymer torque in polymer drag-reduced turbulent channel flows

Kyoungyoun Kim[1,*] and Radhakrishna Sureshkumar[2]
[1]*Department of Mechanical Engineering, Hanbat National University, 125 Dongseo-daero, Yuseong-gu, Daejeon 305-701, South Korea*
[2]*Department of Biomedical and Chemical Engineering, Department of Physics, Syracuse University, New York, 13244, USA*

(Received 6 July 2012; revised manuscript received 14 November 2012; published 4 June 2013)

To study the influence of dynamic interactions between turbulent vortical structures and polymer stress on turbulent friction drag reduction, a series of simulations of channel flow is performed. We obtain self-consistent evolution of an initial eddy in the presence of polymer stresses by utilizing the finitely extensible nonlinear elastic-Peterlin (FENE-P) model. The initial eddy is extracted by the conditional averages for the second quadrant event from fully turbulent Newtonian flow, and the initial polymer conformation fields are given by the solutions of the FENE-P model equations corresponding to the mean shear flow in the Newtonian case. At a relatively low Weissenberg number We_τ (=50), defined as the ratio of the polymer relaxation time to the wall time scale, the generation of new vortices is inhibited by polymer-induced countertorques. Thus fewer vortices are generated in the buffer layer. However, the head of the primary hairpin is unaffected by the polymer stress. At larger We_τ values ($\geqslant 100$), the hairpin head becomes weaker and vortex autogeneration and Reynolds stress growth are almost entirely suppressed. The temporal evolution of the vortex strength and polymer torque magnitude reveals that polymer extension by the vortical motion results in a polymer torque that increases in magnitude with time until a maximum value is reached over a time scale comparable to the polymer relaxation time. The polymer torque retards the vortical motion and Reynolds stress production, which in turn weakens flow-induced chain extension and torque itself. An analysis of the vortex time scales reveals that with increasing We_τ, vortical motions associated with a broader range of time scales are affected by the polymer stress. This is qualitatively consistent with Lumley's time criterion for the onset of drag reduction.

DOI: 10.1103/PhysRevE.87.063002 PACS number(s): 47.57.Ng, 47.85.lb, 47.27.De, 47.27.nd

I. INTRODUCTION

It has been known for more than six decades that the dissolution of minute amounts of high molecular weight polymers in wall-bounded turbulent flows can dramatically reduce turbulent skin friction by up to 70% [1,2]. Experimental studies have revealed many complicated features of polymer drag reduction (DR), such as the onset of DR, the existence of a maximum DR limit, and differences in the modifications of turbulent statistics in the low- and high-DR regimes [3]. However, the mechanism by which the addition of a small amount of long-chain polymers to turbulent pipe or channel flows produces significant turbulent DR is still not fully resolved.

Polymers in solution, when subjected to a flow field, undergo flow orientation, chain stretching, tumbling, and relaxation. The net effect of such configurational changes manifests as an intrinsic elastic stress. The polymer stress in turn influences the flow fields. Flow-configuration coupling in turbulent flows has been numerically investigated by performing direct numerical simulations (DNSs) by employing viscoelastic polymer models such as Oldroyd-B [4], finitely extensible nonlinear elastic-Peterlin (FENE-P) [5–9], and Giesekus [10]. DNS predictions are in qualitative agreement with experimental observations of turbulence statistics in polymer-induced DR in turbulent channel and pipe flows.

DNS results have been used to propose plausible mechanisms of turbulent DR by polymer additives. Sureshkumar *et al.* [9] and Dimitropoulos *et al.* [10,11] proposed a mechanism based on the enhancement of extensional viscosity of the solution caused by chain stretching, which is primarily contributed by the coupling of the fluctuating components of the velocity gradient and conformation tensor. Clear evidence of enhanced streamwise velocity correlations and streak spacing were identified in polymeric channel flows as compared to the Newtonian case. The correlation between velocity fluctuations and polymer-induced body forces was examined by de Angelis *et al.* [5] to show that polymers extract energy from the turbulent fluctuations except in the sublayer, where the viscoelastic force performs positive work on the streamwise component of the turbulent kinetic energy. Min *et al.* [4] derived the transport equation for the kinetic and elastic energies. They showed that the elastic energy stored by polymers in the viscous sublayer is transported to and released in the buffer and log layers when the polymer relaxation time is long enough, thereby significantly reducing the power requirements. Dubief *et al.* [6] explained the positive polymer work performed on the streamwise turbulent structures by proposing a modified autonomous regeneration cycle [12] in which polymer work damps turbulence above the buffer layer and positive polymer work enhances streamwise turbulent intensity in the very near-wall region.

In addition to DNS studies of fully turbulent flows, attempts have been made to understand the DR mechanism using simpler model flows with low Reynolds number. Graham and co-workers [13–16] have extensively studied modifications of the exact coherent state in viscoelastic flows. They suggested that viscoelasticity weakens the streamwise vortices and that the coherent structures can be suppressed entirely if the elastic effects are sufficiently large. Roy *et al.* [17] used a

---

[*] Author to whom correspondence should be addressed: kkim@hanbat.ac.kr

low-dimensional model flow to show that the self-sustaining process becomes weaker because the streak instability is suppressed by polymer forces opposing bi- and uniaxial extension.

While the aforementioned studies of the DR mechanism have focused on the effects of viscoelasticity on the turbulent flow structures in the viscous sublayer and buffer layer, turbulent coherent structures associated with Reynolds shear stress production also exist above the buffer layer [18,19] and their contribution to turbulent drag increases as the Reynolds number increases. At high Reynolds numbers, hairpin vortices are most common in the log layer; they can occur singly but they also occur often in packets. The interaction of the hairpins in the hairpin packet enhances the Reynolds shear stress, for instance, Ganapathisubramani *et al.* [20] showed that the vortex packets contribute about 25% to the total Reynolds shear stress in the log layer while occupying only 4% of the total area. Regarding the effects of viscoelasticity on the outer structures, Kim *et al.* [21] showed that the countertorques created by straining the polymers inherently oppose the rotation of the legs and heads of the hairpins, i.e., the elements responsible for generating much of the Reynolds shear stress in the log layer. The vortex retardation by viscoelastic countertorques has been also observed for quasistreamwise vortices (QSVs) in the buffer layer, and the polymer countertorque concept offers an explanation of the DR mechanism in the outer region of wall turbulence, as well as in the buffer layer.

Recent studies on the Newtonian wall turbulence reveal that large-scale structures in the outer layer have significant contribution to the total Reynolds shear stress and thus turbulent skin friction [22–27]. The large-scale structures consist of vortex organization, i.e., a vortex packet in the log layer [18,20,28–32]. For a mechanism of vortex packet formation, Zhou *et al.* [33,34] proposed an autogeneration process in the Newtonian channel flow. They examined the evolution of the initial field obtained by conditional averages associated with the ejection event. It has been observed that new hairpin vortices are generated upstream of the primary hairpin, thereby forming, together with the upstream hairpins, a coherent packet of hairpins that propagate coherently; this is consistent with the experimental measurements made by high-resolution particle image velocimetry [28]. The autogeneration mechanism has been confirmed by testing for higher Reynolds number flows [35,36] and checking its robustness to the background disturbances [37,38]. Recently, the autogeneration mechanism has been tested for the viscoelastic channel flows by Kim *et al.* [39]. They showed that the autogeneration of new vortices and vortex packet formation are suppressed by viscoelastic effects; thus fewer vortices are observed in DR flows. Combining the weakening of individual vortices by the polymer countertorque and suppression of vortex packet formation, it has been proposed that turbulent DR in viscoelastic flows is caused by decreases in both the coherent and incoherent Reynolds stress.

Kim *et al.* [21] examined the polymer countertorque opposing the vortical motions on the basis of the statistical average. Therefore, to better understand the modification of the near-wall vortices by the polymer torque, it is necessary to investigate the evolution of vortical structures and polymer torques *simultaneously*. Toward this end, we investigated the spatiotemporal evolution of the vortical structures, polymer torque distribution, and Reynolds shear stress profile. Owing to the complexity of vortical structures in fully turbulent flows, we analyzed the evolution of the vortices and polymer torques by tracking the evolution of hairpin vortices, i.e., counter-rotating pairs of QSVs whose nonlinear autogeneration, growth, decay, and breakup are central to turbulent stress production [34].

In this study, we performed a series of dynamical simulations of turbulent channel flow at $\mathrm{Re}_\tau = 395$ in the presence of polymer stresses. By using the FENE-P model, we tracked the self-consistent evolution of the initial vortical structure extracted from fully turbulent Newtonian flow. We examined the three-dimensional distribution of the polymer torque and vortical structures during this evolution at different Weissenberg numbers. We also investigated the time history of the vortex strength and polymer torque magnitude. These studies were used to develop insights into a self-sustaining flow-polymer configuration coupling mechanism that is at the heart of polymer DR. As the Weissenberg number is progressively increased, vortex-polymer torque interactions were observed to influence a progressively broader range of time scales. This observation is used to interpret the time scale criterion for the onset DR proposed by Lumley [40], as well as to understand the asymptotic behavior of DR with increasing Weissenberg number.

II. NUMERICAL METHODS

The evolution of an initially isolated vortical structure in a viscoelastic flow is tracked by performing a dynamical simulation of the channel flow in which the polymer stress is modeled by the FENE-P model. The nondimensional governing equations of unsteady, incompressible, viscoelastic flow of a FENE-P fluid are given by

$$\nabla \cdot \mathbf{u} = 0, \tag{1}$$

$$\frac{\partial \mathbf{u}}{\partial t} + \mathbf{u} \cdot \nabla \mathbf{u} = -\nabla p + \frac{\beta}{\mathrm{Re}_\tau} \nabla^2 \mathbf{u} + \frac{1-\beta}{\mathrm{Re}_\tau} \nabla \cdot \boldsymbol{\tau} + \mathbf{e}_x, \tag{2}$$

$$\frac{\partial \mathbf{c}}{\partial t} + \mathbf{u} \cdot \nabla \mathbf{c} = \mathbf{c} \cdot \nabla \mathbf{u} + (\nabla \mathbf{u})^T \cdot \mathbf{c} - \boldsymbol{\tau}, \tag{3}$$

where $\mathbf{u}$ is the velocity, p is the pressure, and $\boldsymbol{\tau} = ([L^2 - 3]/(L^2 - tr(\mathbf{c}))\mathbf{c} - \mathbf{I})/(\mathrm{We}_\tau/\mathrm{Re}_\tau)$ is the polymer stress [9–11]. The friction velocity u_τ and the channel half height h are used as the velocity and length scale, respectively. A constant mean pressure gradient in the streamwise direction $\mathbf{e}_x = (1, 0, 0)$ is imposed in the momentum equation [Eq. (2)]. The Reynolds number, defined as $\mathrm{Re}_\tau = u_\tau h/\nu_0$, is 395, where ν_0 is the zero-shear-rate kinematic viscosity of the solution. The parameter β is the ratio of the solvent viscosity (μ_s) to the total solution zero-shear-rate viscosity (μ_0). The polymer stress $\boldsymbol{\tau}$ is obtained by solving an evolution equation for the conformation tensor $\mathbf{c}$, which is the average second moment of the polymer chain end-to-end distance vector. L is the maximum extensibility of the polymer molecules. The Weissenberg number We_τ ($=\lambda u_\tau^2/\nu_0$) is the ratio of the polymer relaxation time λ to the flow time scale based on the friction velocity.

Because the second quadrant (Q2) turbulent events play a dominant role in Reynolds shear stress production in wall-bounded turbulence [28,41], we have examined the evolution of vortical structures associated with the Q2 event vector. The initial vortical structure is extracted from the conditional averaged flow field in the Q2 event in the DNS data for fully developed Newtonian turbulent channel flow at $\mathrm{Re}_\tau = 395$ [38],

$$\mathbf{u}(\mathbf{x},t=0) = \bar{\mathbf{u}}(y) + \langle \mathbf{u}'(\mathbf{x}) | \mathbf{u}'(y_m) = \alpha(u_m, v_m, 0)\rangle, \tag{4}$$

where the overbar denotes a time average. The amplification factor α here refers to the strength of the Q2 event. The events (u_m, v_m) are chosen as the Q2 event which maximize the probability-weighted Reynolds shear stress $u'v'$ pdf(u', v') and thereby maximize the contribution to the mean Reynolds shear stress, since $\overline{u'v'} = \int\int u'v' \,\mathrm{pdf}(u',v')du'dv'$ [42]. The conditional average is approximately calculated from the linear stochastic estimation procedure described in [43]. The linear stochastic approximation of the conditional average $\langle u_i | E_j \rangle$ is written as

$$u_i(\mathbf{x}) = L_{ij}(\mathbf{x};\mathbf{x}')E_j(\mathbf{x}'). \tag{5}$$

Choosing L_{ij} to minimize the mean square error yields equations for L_{ij} in terms of unconditional, two-point, second-order spatial correlation tensors:

$$\langle E_j(\mathbf{x}')E_k(\mathbf{x}')\rangle L_{ij} = \langle u_i(\mathbf{x})E_k(\mathbf{x}')\rangle. \tag{6}$$

From Eq. (5), the linear estimate of the conditional average $\langle u_i'(\mathbf{x}) | \alpha(u_m, v_m, 0)\rangle$ in Eq. (4) reduces to

$$u_i'(\mathbf{x}) = L_{i1}\alpha u_m(y_m) + L_{i2}\alpha v_m(y_m), \tag{7}$$

with $i = 1$, 2, and 3 and

$$\begin{bmatrix} L_{i1} \\ L_{i2} \end{bmatrix} = \begin{bmatrix} \langle u'^2\rangle(y_m) & \langle u'v'\rangle(y_m) \\ \langle u'v'\rangle(y_m) & \langle v'^2\rangle(y_m) \end{bmatrix}^{-1} \begin{bmatrix} \langle u_i'(\mathbf{x})u'(y_m)\rangle \\ \langle u_i'(\mathbf{x})v'(y_m)\rangle \end{bmatrix}, \tag{8}$$

which approximates conditional averages in a form that is computationally convenient, since it depends only on two-point correlation tensors. The accuracy of LSE as an approximation to conditional average has been confirmed elsewhere [44].

The initial polymer conformation field is given by the solutions of the FENE-P model equations for the mean shear flow in the Newtonian case [9]:

$$C_{xx}^{MF} = \frac{1}{F(y)}\left\{1 + \frac{2\mathrm{We}_h^2}{F(y)^2}\left(\frac{dU}{dy}\right)^2\right\}, \quad C_{xy}^{MF} = \frac{\mathrm{We}_h}{F(y)^2}\frac{dU}{dy},$$
$$C_{yy}^{MF} = C_{zz}^{MF} = \frac{1}{F(y)}, \quad C_{xz}^{MF} = C_{yz}^{MF} = 0, \tag{9}$$

where

$$F(y) = \frac{\sqrt{3}\Omega(y)}{2\sinh(\phi/3)}, \quad \Omega(y) = \frac{\sqrt{2}\mathrm{We}_h}{L}\frac{dU}{dy},$$
$$\phi = \sinh^{-1}(3\sqrt{3}\Omega/2), \ \mathrm{We}_h = \lambda u_\tau/h = \mathrm{We}_\tau/\mathrm{Re}_\tau.$$

Here, y is the wall-normal direction and $U(y)$ is the mean streamwise velocity.

The governing equations are time integrated by using a semi-implicit method similar to that in Beris and Sureshkumar [45]. The spatial derivatives are obtained by using a spectral method with Fourier representations in the streamwise and spanwise directions, and Chebyshev expansion in the wall-normal direction. Periodic boundary conditions are applied in the streamwise and spanwise directions, and the no-slip boundary condition is imposed on the velocity at the solid walls. More details on the numerical method are available in Sureshkumar *et al.* [9]. The domain size is $4\pi h \times 2h \times \pi h$ in the streamwise, wall normal, and spanwise directions, respectively. Note that the longer streamwise length of the simulation box is necessary to account for enhanced streamwise velocity correlations that exist in the viscoelastic cases. After testing several grid resolutions [39,46], we chose to use $256 \times 128 \times 192$ spectral modes; as a result, $\Delta x^+ = 19.4$, $\Delta y^+ = 0.12 \sim 9.69$, and $\Delta z^+ = 6.46$, where the superscript $+$ indicates quantities nondimensionalized by wall variables u_τ and ν_0.

III. RESULTS AND DISCUSSION

Figure 1 shows several snapshots of the evolution of the initial vortical structure in viscoelastic flows at three different Weissenberg numbers ($\mathrm{We}_\tau = 50$, 100, and 200). Vortices are identified using the swirling strength (λ_{ci}), defined as the absolute value of the imaginary part of the complex conjugate eigenvalues of the local velocity gradient tensor [34,47]. The initial vortex was extracted by the Q2 event of $\alpha = 3$ specified at $y^+ = 50$ from the Newtonian flow simulations. The other rheological parameters of the FENE-P model were $\beta = 0.9$ and $L = 120$. Note that the friction velocity used for the velocity normalization for the viscoelastic flows is the same as that for Newtonian flow, because the same constant mean pressure gradient is imposed for both cases.

The evolution of the same initial vortex in the Newtonian flow is also displayed in Fig. 1(a) for comparison. The initial vortical structure is changed to an Ω-shaped vortex at t^+ ($= tu_\tau^2/\nu_0$) $= 79$ by self-induced motion in the binormal direction due to the local effect of the curved vortex line [34]. A secondary hairpin vortex ($t^+ = 158$) is generated upstream of the primary hairpin vortex, and the vortices move downstream with almost the same convection velocity and little dispersion, forming a vortex packet. Subsequently, new vortices in the buffer layer are also generated upstream of the secondary vortices.

The autogeneration of new vortices is clearly suppressed in the viscoelastic flows. At a relatively low Weissenberg number ($\mathrm{We}_\tau = 50$), the generation of new vortices is inhibited by the polymer stress; consequently, fewer vortices appear in the buffer layer. However, the head of the primary hairpin is unaffected by the polymer stress as compared with that in the Newtonian flow [Fig. 1(a)]. At higher We_τ values (100 and 200), the hairpin head and legs both weaken, and autogeneration of new vortices is not observed. The weakening of the primary hairpin vortex becomes more significant as We_τ increases, and thus the time scale over which the vortex disappears is shortened. Moreover, the wall-normal extent of vortex weakening increases with We_τ.

Figure 2 shows profiles of the Reynolds shear stress averaged in the horizontal (x-z) plane at several instants. Because the Reynolds shear stress profile is expected to be closely related to the vortex evolution, vortical structures in the Newtonian flow are also shown for reference. Because the initial flow field is imposed as the conditionally averaged velocities with Q2 event specified at $y^+ = 50$ ($y/h = 0.13$),

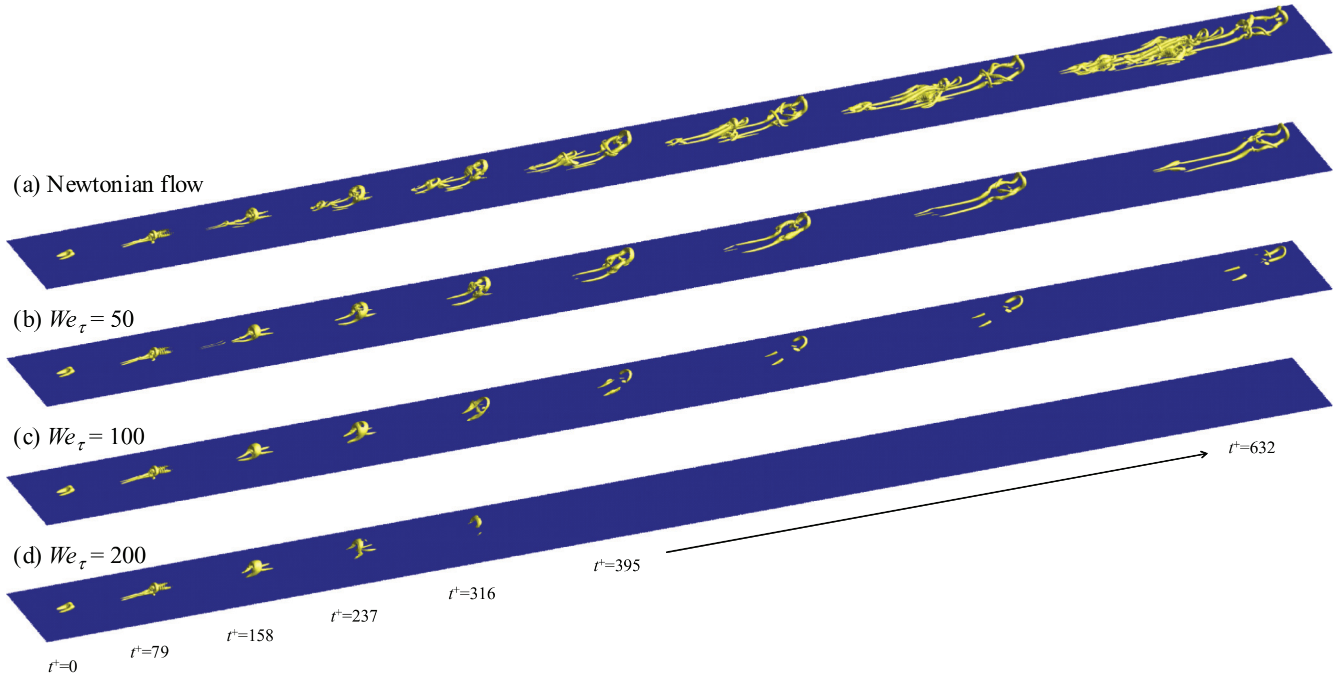

FIG. 1. (Color online) Snapshots of the evolution of initial vortical structure extracted by Q2 event vector of strength $\alpha = 3$ specified at $y^+ = 50$ from Newtonian flow in (a) Newtonian and (b)–(d) viscoelastic flows. Vortices are visualized using the isosurfaces of 20% of the maximum swirling strength (λ_{ci}) of the initial eddy.

the Reynolds shear stress profiles have a peak at the Q2 event location as shown in Fig. 2(a). At $t^+ = 79$ [Fig. 2(b)], the peak moves away from the wall since the initial vortex is lifted up with forming the Ω-shaped primary hairpin vortex. However, the viscoelastic effects on the Reynolds shear stress profile are negligible in this early stage of the evolution ($t^+ < 79$) and the effects begin to be clearly observed from $t^+ = 158$ [Fig. 2(c)].

In the Newtonian flow, at $t^+ = 237$, a local maximum located near the wall ($y/h = 0.1$) is observed which is

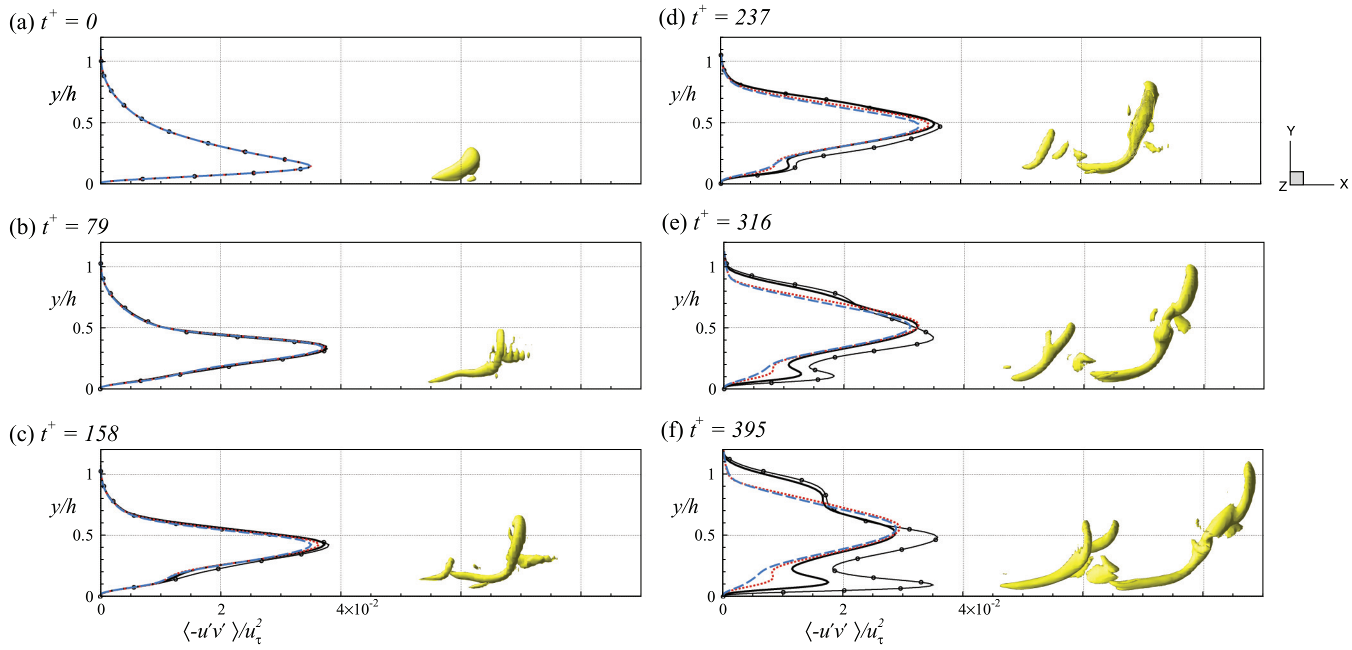

FIG. 2. (Color online) Profiles of the Reynolds shear stress during the evolution of the initial structure extracted by Q2 event vector of strength $\alpha = 3$ specified at $y^+ = 50$ in the Newtonian flow. Vortical structures in the Newtonian flow are also shown for reference. To better visualize the hairpin, the y direction is scaled up by a factor of 2. Solid line with symbols: Newtonian flow; solid lines: $\mathrm{We}_\tau = 50$; dotted lines: $\mathrm{We}_\tau = 100$; dashed lines: $\mathrm{We}_\tau = 200$.

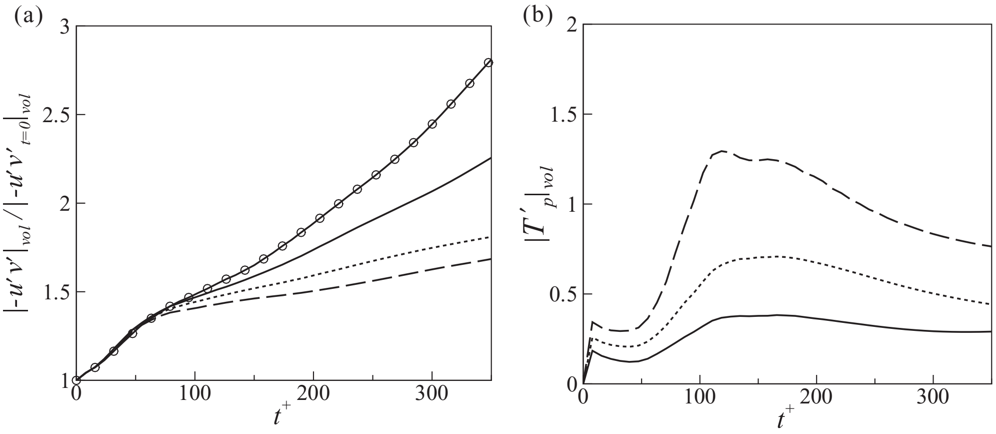

FIG. 3. Growth rate of volume-averaged values during the evolution of the initial structure extracted by Q2 event vector of strength $\alpha = 3$ specified at $y^+ = 50$ in Newtonian flow. (a) Reynolds shear stress; (b) polymer torque magnitude. Solid line with symbols: Newtonian flow; solid lines: $\mathrm{We}_\tau = 50$; dotted lines: $\mathrm{We}_\tau = 100$; dashed lines: $\mathrm{We}_\tau = 200$.

associated with new vortices generated upstream of the primary hairpin and the strengthening of the primary vortex legs due to vortex stretching near the wall. The outer peak at $y/h \approx 0.45$ corresponds to the head of the primary hairpin vortex. The secondary vortex head is lifted upward with time because of the Q2 pumping induced by the primary hairpin vortex. The lifted secondary hairpin head makes an additional contribution to the Reynolds shear stress associated with the primary hairpin, producing a peak near $y/h = 0.5$ at $t^+ = 395$ [Fig. 2(f)]. At the same time, the primary hairpin spreads farther from the wall with decreased strength due to viscous diffusion, causing a diffuse shoulder near $y/h = 0.8$ in Fig. 2(f). The maximum observed near $y/h = 0.1$ at $t^+ = 237$ becomes a larger peak at $t^+ = 395$ because the vortex legs near the wall are further strengthened by vortex stretching by the high mean shear.

At relatively low We_τ (=50), the variations in the Reynolds shear stress with time are similar to those in the Newtonian flow. In Fig. 2(f), the near-wall peak value of the Reynolds shear stress is lower, whereas the profiles are nearly the same as that for the Newtonian flow at $y/h > 0.6$. This is consistent with the observation in Fig. 1(b) that fewer vortices appear in the buffer layer because the autogeneration process is inhibited by polymer stress, but the head of the primary hairpin is unaffected. At larger We_τ values ($\geqslant 100$), the near-wall peaks are significantly suppressed compared with those in the Newtonian flow. In Fig. 2(f), the diffuse shoulder in the outer layer associated with the primary hairpin vortex head, observed in both the Newtonian and $\mathrm{We}_\tau = 50$ flows, disappears. This is consistent with the suppression of the eddies at higher Weissenberg numbers as shown in Fig. 1. Overall, the variation in the Reynolds shear stress profiles during vortex evolution in viscoelastic flows reported here corroborates DNS and experimental results for fully turbulent drag-reduced flows, in that the Reynolds shear stress is reduced only in the buffer layer for low DR (LDR), whereas for high DR (HDR), it is also reduced in the outer layer [3,7,8,48].

Figure 3(a) shows the volume-averaged Reynolds shear stress normalized with respect to its initial value during the evolution of the initial vortex. The growth rate of the volume-averaged Reynolds shear stress decreases as We_τ increases owing to the inhibited autogeneration mechanism and weakened vortices (Fig. 1). Further, a closer examination reveals that the viscoelastic effects are manifested more rapidly in time as the Weissenberg number increases. The Reynolds shear stress of the viscoelastic flows begin to deviate from that for the Newtonian flow by more than 5% at $t^+ = 163$, 122, and 98 for $\mathrm{We}_\tau = 50$, 100, and 200, respectively. The more rapid manifestation of viscoelastic effects in the Reynolds shear stress for higher We_τ is consistent with evolution of vortical structures in Fig. 1; with increasing We_τ, the vortical structures are weakened more rapidly, resulting in decreased production of turbulent stresses. In fully turbulent drag-reduced flows, the lower values of Reynolds shear stress compared with Newtonian flows have been attributed to weakened vortices because the polymer torque due to the polymer stress acts against the vortical motion of the near-wall vortices [21].

Figure 3(b) shows the temporal evolution of the volume-averaged polymer torque magnitude. The polymer torque ($\mathbf{T}_p$) is defined as the curl of the polymer force vector ($\mathbf{f}_p$) as

$$\mathbf{T}_p = \nabla \times \mathbf{f}_p = \nabla \times \left(\frac{1-\beta}{\mathrm{Re}_\tau} \nabla \cdot \boldsymbol{\tau} \right).$$

Because the initial condition corresponds to polymers prestretched by the mean shear, the polymer torque begins to affect the flow in the early stages of vortex evolution. The polymer torque magnitude increases as We_τ increases, which suggests that a higher We_τ induces a larger polymer torque against the vortical motions, and thus produces greater vortex weakening. The polymer torque decreases very early on during its evolution ($t^+ < 50$); during this phase, the polymer torque is concentrated on the initial vortex, which develops into an Ω-shaped vortex by self-induced motion due to local curvature effects. The polymer torque subsequently increases, reaching a maximum at around $t^+ = 100$; at this time, a secondary vortex is generated upstream of the primary hairpin in the Newtonian flow. This large polymer torque inhibits autogeneration in the viscoelastic flow by suppressing the vortical motions of the primary hairpin. The polymer torque decreases after $t^+ \approx 200$, which can be attributed to the decrease in the vorticity magnitude after autogeneration,

(a) $\mathrm{We}_\tau = 50$

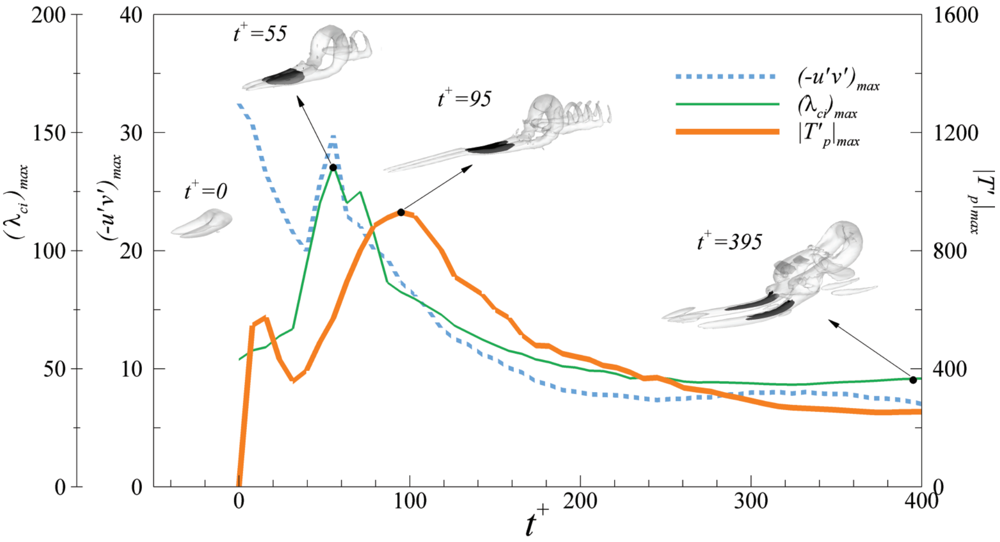

(b) $\mathrm{We}_\tau = 100$

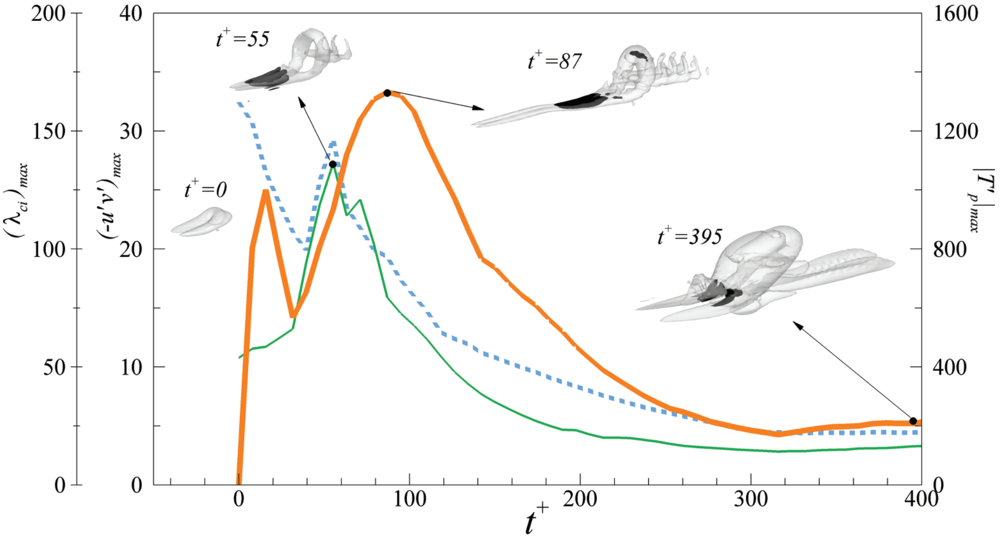

FIG. 4. (Color online) Temporal variations in maximum values of vortex swirling strength and polymer torque magnitude. To visualize the region of large polymer torque, the isosurface (dark gray) of 50% of $|T'_p|_{\mathrm{max}}$ is shown around the vortical structures (light gray) described by the isosurface of 20% of $\lambda_{ci,\mathrm{max}}$.

since the weakened vortices induce less polymer stretching and thus a weaker polymer torque.

To elucidate the self-consistent interactions between the polymer torque and the changes in the Reynolds shear stress during vortex evolution, the temporal variations in the maximum values of the Reynolds shear stress and polymer torque magnitude are displayed in Fig. 4. The time history of the maximum vortex swirling strength is also shown, and the vortical structures at several instants are visualized using the isosurface corresponding to 20% of the maximum λ_{ci} in order to obtain a visual signature of the vortex modification process.

The time histories of the local maximum of the Reynolds shear stress show that $(-u'v')_{\mathrm{max}}$ decreases as evolution begins, whereas the volume-averaged values increase monotonically from the initial state [Fig. 3(a)]. The reason is that as the initially confined vortex grows and develops into larger-scale flow structures, the cumulative Reynolds shear stress produced by vortical motions increases, although the local maximum value decreases. When the initial vortex forms an Ω-shaped primary hairpin vortex ($t^+ \approx 55$), the Reynolds shear stress reaches a maximum; it then decreases along with the vortex strength because of the increased polymer countertorque. The maximum values of the polymer torque magnitude $|\mathbf{T}'_p|_{\mathrm{max}}$ increase abruptly from zero and show a subsequent decrease; they then increase again, peaking at $t^+ \approx 95$ and 87 for $\mathrm{We}_\tau = 50$ and 100, respectively, and then decrease. The overall behaviors of the local maximum $|\mathbf{T}'_p|$ are similar to those of the volume-averaged values, $|\mathbf{T}'_p|_{\mathrm{vol}}$ as shown in Fig. 3(b).

The maximum vortex swirling strength $\lambda_{\mathrm{ci,max}}$ first increases from its initial value until $t^+ \approx 55$ and then decreases.

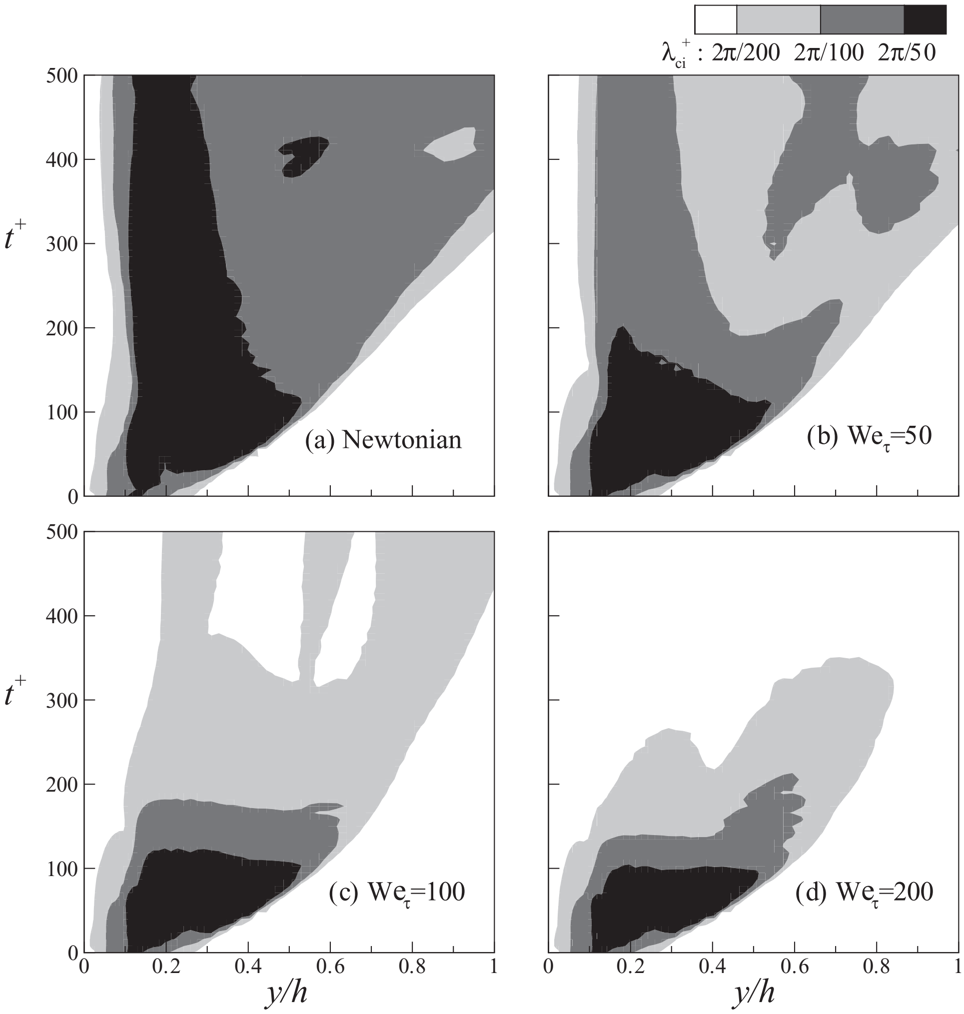

FIG. 5. Spatiotemporal evolution of maximum swirling strength in the x-z plane, $\max(\lambda_{ci}^+)_{xz}$. Three contour levels are shown: max $(\lambda_{ci}^+)_{xz} = 2\pi/\mathrm{We}_\tau$ at $\mathrm{We}_\tau = 50$ (black), 100 (gray), and 200 (light gray).

Note that the increase in the polymer torque magnitude follows by an increase in the vortex swirling strength. This suggests that the increase in vortex strength produces higher straining motion near the vortices, which results in greater polymer stretching and, in turn, an increase in the polymer torque acting on the vortices in the direction opposite to the vortical motion. The stronger polymer torque at $\mathrm{We}_\tau = 100$ causes the vortex swirling strength and Reynolds shear stress to decrease more rapidly after the primary hairpin vortex forms ($t^+ > 55$) than at $\mathrm{We}_\tau = 50$.

To identify the regions in which high polymer torque occurs near the vortices, the isosurface of 50% of $|\mathbf{T}'_p|_{\max}$ around the vortical structures is shown in dark shades in Fig. 4. The initial vortex changes significantly during the polymer relaxation time at $\mathrm{We}_\tau = 50$ (or earlier at $\mathrm{We}_\tau = 100$) and develops to an Ω-shaped vortex at $t^+ \approx 55$ when $\lambda_{\mathrm{ci,max}}$ becomes largest during the vortex evolution. The isosurface corresponding to 50% of $|\mathbf{T}'_p|_{\max}$ reveals that the regions of high polymer torque are concentrated in the vortex legs, which retards ejection motions between the vortex legs by opposing vortical motions of the legs, and thus suppresses the generation of a secondary hairpin vortex. Although the vortices at different We_τ values are similar when $|\mathbf{T}'_p|_{\max}$ is the largest during vortex evolution, the distributions of the polymer torque differ. At $\mathrm{We}_\tau = 100$, a large polymer countertorque is observed in the hairpin vortex head as well as the legs, whereas a strong polymer torque is observed only in the vortex legs at $\mathrm{We}_\tau = 50$. Because of the large countertorque in the hairpin head, the head weakens at $\mathrm{We}_\tau = 100$ and is diffused and elongated in the streamwise direction compared with that at $\mathrm{We}_\tau = 50$. Since the polymer torque at $\mathrm{We}_\tau = 50$ is confined to the inner layer during vortex evolution, the vortices in the outer layer are unaffected by viscoelasticity at $\mathrm{We}_\tau = 50$ compared with those obtained from the Newtonian simulation (Fig. 1).

According to Lumley's criterion for the onset of DR, polymers can affect the flow only when the polymer relaxation time is larger than a suitably defined flow time scale [40]. Because the vortex swirling strength is related to the inverse of the vortex time scale, $t_{\mathrm{vortex}} \sim 2\pi/\lambda_{ci}$ [47], vortices having a smaller time scale than the polymer relaxation time ($t^+_{\mathrm{vortex}} \sim 2\pi/\lambda^+_{ci} < \mathrm{We}_\tau$), i.e., vortical motions with sufficiently high swirling strength ($\lambda^+_{ci} > 2\pi/\mathrm{We}_\tau$), are expected to be affected by polymers. In other words, as We_τ increases, vortices having a wider range of swirling strengths can be affected

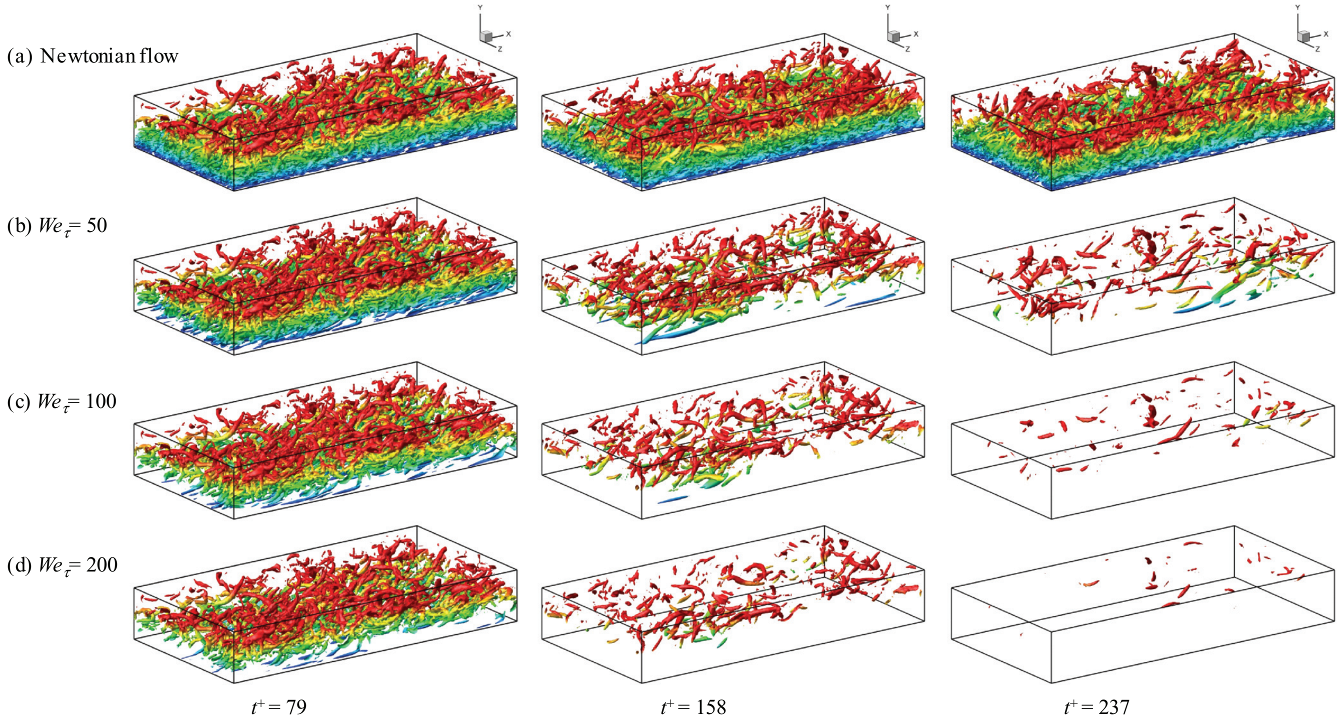

FIG. 6. (Color) Evolution of initially fully turbulent vortical structures in (a) Newtonian and (b)–(d) viscoelastic flows. The vortices are shown as colored isosurfaces 5% of the maximum swirling strength (λ_{ci}) of the initial flow field. Blue and red color indicate vortices closer to and farther from the wall, respectively.

by polymer stress. To observe the relationship between the polymer relaxation time and the vortex swirling strength, the spatiotemporal evolution of $\lambda_{ci,\max}$ in the horizontal plane x-z is shown in Fig. 5. Three contour levels for λ_{ci}^+ are shown over which vortices have a time scale smaller than the polymer relaxation time at $\mathrm{We}_\tau = 50$, 100, and 200, respectively. At $t^+ < 100$, the distributions of $\lambda_{ci,\max}$ in viscoelastic flows are nearly the same as in the Newtonian flow; this time interval corresponds to the formation of an Ω-shaped vortex from the initial vortex (Fig. 1). However, viscoelastic effects appear after $t^+ \approx 100$. In the Newtonian flow [Fig. 5(a)], a high swirling strength (denoted by black shade) continues to be observed near the wall over time; this is associated with the autogenerated vortices. At $\mathrm{We}_\tau = 50$ [Fig. 5(b)], the region in which λ_{ci}^+ is larger than $2\pi/\mathrm{We}_\tau$ (black) disappears entirely at $t^+ > 200$. At $\mathrm{We}_\tau = 100$ and 200, the region at which $\lambda_{ci}^+ > 2\pi/\mathrm{We}_\tau$ disappears at $t^+ \approx 185$ and 350, respectively [Figs. 5(c) and 5(d)]. This suggests that at larger Weissenberg numbers, vortical motions associated with a broader range of time scales are affected by the polymer stress, which is consistent with Lumley's time criteria for the onset of DR. Consequently, for a given Reynolds number, as the Weissenberg number is increased, the viscoelastic effects eventually encompass all dynamically relevant vortex time scales and hence the DR saturates, consistent with experimental observations [49].

Note that the discussion so far has been based on the spatiotemporal modification by viscoelastic torques of a single conditionally averaged hairpin vortex, whereas in real turbulent flows, numerous vortices of varying spatial scales at different phases of formation, growth, and decay are populated and interact with one another. Further, smaller scale motions also exist within the flow field. In order to evaluate whether the physical insights gleaned by observing the evolution of the conditional eddy are relevant to the entire flow field, dynamical simulations were performed to study the effect of polymer-induced stresses on the evolution of the fully turbulent flow field from which the initial hairpin eddy was extracted. Specifically, the initial velocity field is given by an instantaneous flow field taken from the DNS of fully turbulent Newtonian channel flow at $\mathrm{Re}_\tau = 395$. The initial polymer conformation tensor field is obtained by solving Eq. (9) as in the case of single vortex simulations. Domain sizes of $2\pi h$ and πh were used in the streamwise and spanwise directions, respectively, along with a $128 \times 129 \times 192$ grid. Other simulation parameters are $L = 14\,400$, $\beta = 0.9$, and $\mathrm{We}_\tau = 50, 100, 200$.

Figure 6 shows several snapshots of vortical structures during the evolution of the initial fully turbulent flow field for the Newtonian and viscoelastic cases. The vortical structures are identified as colored isosurfaces of the vortex swirling strength and the color is progressively changed from blue to red as the distance of the vortex core from the wall increases. In the Newtonian flow, relatively weak arch-shaped or spanwise vortices are populated in the outer layer, while quasistreamwise vortices become dominant close to the wall. On the other hand, in the viscoelastic flows, the vortices become weaker as time progresses and it is clearly observed that *inner vortices are weakened first and eventually suppressed*. Further, within a given time interval, the extent in the wall-normal direction of

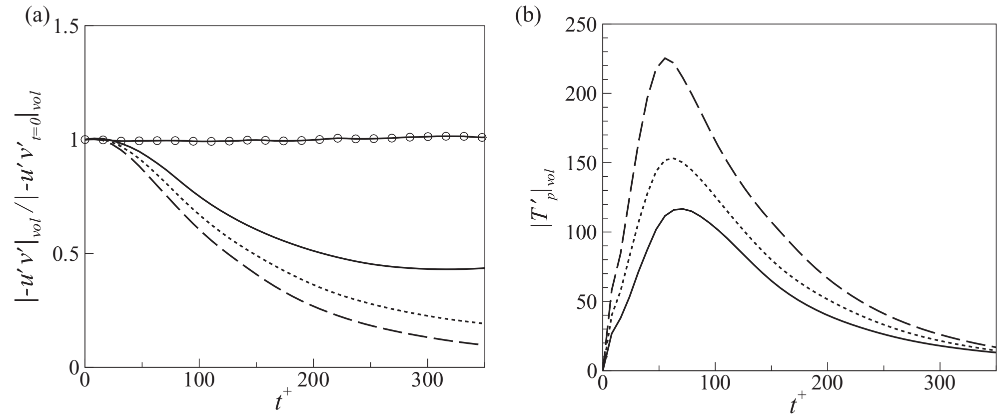

FIG. 7. Temporal variations of volume-averaged values during the evolution of fully turbulent flow field. (a) Reynolds shear stress; (b) polymer torque magnitude. Solid line with symbols: Newtonian flow; solid lines: $\mathrm{We}_\tau = 50$; dotted lines: $\mathrm{We}_\tau = 100$; dashed lines: $\mathrm{We}_\tau = 200$.

vortex weakening due to viscoelastic effects increases as We_τ increases. These observations for a fully turbulent flow are consistent with those obtained from the dynamics simulations of a conditional eddy (Fig. 1).

Figure 7 shows temporal changes of the volume-averaged Reynolds shear stress and polymer torque magnitude during the evolution of the fully turbulent flow field. As shown in Fig. 7(a), the volume-averaged Reynolds shear stress decays in the viscoelastic flows and the decay rate increases with increasing We_τ, which is consistent with the results obtained from the single vortex evolution [Fig. 3(a)], indicating that viscoelastic effects are manifested more rapidly in time as We_τ is increased. Figure 7(b) shows that the temporal changes in the volume-averaged polymer torque magnitude are also similar to those observed in the single vortex evolution [Fig. 3(b)]: $|\mathbf{T}'_p|_{\mathrm{vol}}$ is larger for larger We_τ, and it increases and reaches a maximum at around $t^+ \approx 60$, which is somewhat earlier than that for the conditionally averaged vortex evolution ($t^+ \approx 100$). Note that in the single vortex evolution $\mathbf{T}'_p|_{\max}$ occurs at around the time when the secondary vortex is generated, and this occurs faster for stronger initial vortex [34]. In the fully turbulent initial condition, the initial vortex strength is larger than that for the single hairpin eddy, i.e., the vortex swirling strength $\lambda_{ci}h/u_\tau = 18$ and 11 in the fully turbulent flow and single hairpin, respectively. Hence the earlier occurrence of $\mathbf{T}'_p|_{\max}$ in fully turbulent flow evolution is not surprising. After $t^+ \approx 60$, $|\mathbf{T}'_p|_{\mathrm{vol}}$ decreases monotonically, which can be attributed to decreased levels of polymer stretch due to the weakened vortices as discussed in Fig. 3(b).

DNS and experimental studies of wall-bounded turbulent flows have revealed that QSVs are dominant in the inner layer, and hairpin or arch-type vortices are dominant in the outer layer [18,19]. In addition, the vortices in the outer layer are reportedly weaker than those in the inner layer. In this context, the present results suggest that in viscoelastic flows with a polymer relaxation time that is small but larger than the vortex time scale of the strongest vortices near the wall, near-wall vortices can be affected by the polymer stress, whereas weaker vortices in the outer layer remain unaffected. For polymer relaxation times larger than the vortex time scale associated with the weak outer vortices, entire vortices in the flow can be modified, changing the flow characteristics of both the outer and inner layers. The interplay between the vortex time scale and polymer relaxation time can help explain the differences in the flow characteristics between the LDR regime realized at relatively small Weissenberg numbers and the HDR regime observed at larger We_τ; e.g., the mean velocity in the log layer has the same slope as in Newtonian flow for LDR but is higher for HDR [48].

IV. CONCLUSION

The effect of dynamic interactions between turbulent vortical structures and polymer stress on turbulent friction DR was examined by performing a series of spectral simulations for channel flow at $\mathrm{Re}_\tau = 395$. By using the FENE-P model, we obtained self-consistent evolution of the initial vortical structure in the presence of polymer stresses.

At a relatively low Weissenberg number ($\mathrm{We}_\tau = 50$), the generation of new vortices is inhibited by polymer-induced countertorque, so fewer vortices appear in the buffer layer. However, the head of the primary hairpin is unaffected by the polymer stress. At larger We_τ values ($\geqslant 100$), the hairpin head weakens, and vortex autogeneration is almost entirely suppressed. Moreover, as We_τ increases, vortices in both the outer layer and the buffer layer are affected by the polymer stress. In agreement with the vortex evolution, the Reynolds shear stress profile at low We_τ is affected by the polymer stress only in the buffer layer, whereas at higher We_τ, the viscoelastic effects extend to the outer layer.

We showed that at $\mathrm{We}_\tau = 50$, the polymer countertorque is concentrated on the hairpin vortex legs in the buffer layer, which suppresses autogeneration of new vortices. With increasing Weissenberg number, a large polymer countertorque is observed in the hairpin head as well as the vortex legs, which weakens the outer-layer vortices. The time history of the vortex strength and polymer torque magnitude revealed that a strong polymer torque is generated by strong vortical motions after a time delay, inducing polymer stretching; in turn, the increased polymer torque retards the vortical motions. Finally, we examined the changes in the vortex time scales and found that with increasing Weissenberg number, vortical motions associated with a wider range of time scales are affected by the polymer stress, in agreement with Lumley's time criteria for the onset of DR.

Although a clear relationship between the nonlinear evolution of the mean and the mean of the nonlinear evolution may not exist for highly nonlinear systems, the present exploration has led, *a posteriori*, to the following mechanisms that are closely related to the evolution of the nonlinear system itself, which has been studied by DNS: In viscoelastic flows with a polymer relaxation time that is small but larger than the vortex time scale of the strongest vortices near the wall, near-wall vortices can be affected by the polymer stress, whereas weaker vortices in the outer layer remain unaffected. As the polymer relaxation time is progressively increased, the eddy structures with longer time scales interact with the polymer and the outer-layer modification becomes more pronounced. The interplay between the vortex time scale and polymer relaxation time can help explain the differences in the flow characteristics between the LDR regime realized at relatively small Weissenberg numbers and the HDR regime observed at larger Weissenberg number. Furthermore, the existence of maximum DR limit can be explained; for a given Reynolds number, as the Weissenberg number is increased, the viscoelastic effects eventually encompass all dynamically relevant vortex time scales and hence the DR saturates.

ACKNOWLEDGMENTS

This research was supported by the Basic Science Research Program through the National Research Foundation of Korea (NRF), funded by the Ministry of Education, Science and Technology (Project No. 2010-0007901) (K.K.), and a NSF CBET grant (Grant No. 1055219) (R.S.).

---

[1] B. A. Toms, in *Proc. of the 1st Int. Congress of Rheology* (North Holland, Amsterdam, 1948), p. 135.
[2] B. A. Toms, Phys. Fluids **20**, 3 (1977).
[3] C. M. White and M. G. Mungal, Annu. Rev. Fluid Mech. **40**, 235 (2008).
[4] T. Min, J. Y. Yoo, H. Choi, and D. D. Joseph, J. Fluid Mech. **486**, 213 (2003).
[5] E. De Angelis, C. M. Casciola, and R. Piva, Comput. Fluid **31**, 495 (2002).
[6] Y. Dubief, C. M. White, V. E. Terrapon, E. S. G. Shaqfeh, P. Moin, and S. K. Lele, J. Fluid Mech. **514**, 271 (2004).
[7] C.-F. Li, R. Sureshkumar, and B. Khomami, J. Non-Newton. Fluid **140**, 23 (2006).
[8] P. K. Ptasinski, B. J. Boersma, F. T. M. Nieuwstadt, M. A. Hulsen, B. Van den Brule, and J. C. R. Hunt, J. Fluid Mech. **490**, 251 (2003).
[9] R. Sureshkumar, A. N. Beris, and R. A. Handler, Phys. Fluids **9**, 743 (1997).
[10] C. D. Dimitropoulos, R. Sureshkumar, and A. N. Beris, J. Non-Newton. Fluid **79**, 433 (1998).
[11] C. D. Dimitropoulos, R. Sureshkumar, A. N. Beris, and R. A. Handler, Phys. Fluids **13**, 1016 (2001).
[12] J. Jiménez and A. Pinelli, J. Fluid Mech. **389**, 335 (1999).
[13] W. Li and M. D. Graham, Phys. Fluids **19**, 083101 (2007).
[14] W. Li, L. Xi, and M. D. Graham, J. Fluid Mech. **565**, 353 (2006).
[15] P. A. Stone, A. Roy, R. G. Larson, F. Waleffe, and M. D. Graham, Phys. Fluids **16**, 3470 (2004).
[16] P. A. Stone, F. Waleffe, and M. D. Graham, Phys. Rev. Lett. **89**, 208301 (2002).
[17] A. Roy, A. Morozov, W. van Saarloos, and R. G. Larson, Phys. Rev. Lett. **97**, 234501 (2006).
[18] R. J. Adrian, Phys. Fluids **19**, 041301 (2007).
[19] S. K. Robinson, Annu. Rev. Fluid Mech. **23**, 601 (1991).
[20] B. Ganapathisubramani, E. K. Longmire, and I. Marusic, J. Fluid Mech. **478**, 35 (2003).
[21] K. Kim, C. F. Li, R. Sureshkumar, S. Balachandar, and R. J. Adrian, J. Fluid Mech. **584**, 281 (2007).
[22] B. Balakumar and R. Adrian, Philos. Trans. R. Soc. London A **365**, 665 (2007).
[23] M. Guala, S. Hommema, and R. Adrian, J. Fluid Mech. **554**, 521 (2006).
[24] J. H. Lee and H. J. Sung, J. Fluid Mech. **673**, 80 (2011).
[25] I. Marusic, Phys. Fluids **13**, 735 (2001).
[26] J. P. Monty, J. A. Stewart, R. C. Williams, and M. S. Chong, J. Fluid Mech. **589**, 147 (2007).
[27] X. Wu, J. R. Baltzer, and R. J. Adrian, J. Fluid Mech. **698**, 235 (2012).
[28] R. J. Adrian, C. D. Meinhart, and C. D. Tomkins, J. Fluid Mech. **422**, 1 (2000).
[29] K. T. Christensen and R. J. Adrian, J. Fluid Mech. **431**, 433 (2001).
[30] B. Ganapathisubramani, N. Hutchins, W. T. Hambleton, E. K. Longmire, and I. Marusic, J. Fluid Mech. **524**, 57 (2005).
[31] K. C. Kim and R. J. Adrian, Phys. Fluids **11**, 417 (1999).
[32] I. Marusic, B. J. McKeon, P. A. Monkewitz, H. M. Nagib, A. J. Smits, and K. R. Sreenivasan, Phys. Fluids **22**, 065103 (2010).
[33] J. Zhou, R. J. Adrian, and S. Balachandar, Phys. Fluids **8**, 288 (1996).
[34] J. Zhou, R. J. Adrian, S. Balachandar, and T. M. Kendall, J. Fluid Mech. **387**, 353 (1999).
[35] G. Elsinga, M. G. Vishwanathappa, and W.-P. Breugem, in *65th Annual Meeting of the APS Division of Fluid Dynamics* (American Physical Society, New York, 2012); http://meetings.aps.org/link/BAPS.2012.DFD.D20.3.
[36] K. Kim, in *65th Annual Meeting of the APS Division of Fluid Dynamics* (American Physical Society, New York, 2012); http://meetings.aps.org/link/BAPS.2012.DFD.F1.97.
[37] R. Adrian and Z. Liu, J. Visualization **5**, 9 (2002).
[38] K. Kim, H. J. Sung, and R. J. Adrian, Phys. Fluids **20**, 105107 (2008).
[39] K. Kim, R. J. Adrian, S. Balachandar, and R. Sureshkumar, Phys. Rev. Lett. **100**, 134504 (2008).
[40] J. L. Lumley, Annu. Rev. Fluid Mech. **1**, 367 (1969).
[41] J. Kim, P. Moin, and R. Moser, J. Fluid Mech. **177**, 133 (1987).
[42] P. Moin, R. J. Adrian, and J. Kim, in *Proc. of the 6th Turbulent Shear Flow Symposium* (Pennsylvania State University, University Park, 1987), p. 16.9.1.

[43] R. J. Adrian, in *Eddy Structure Identification*, edited by J. P. Bonnet (Springer, New York, 1996), p. 145.

[44] R. J. Adrian, B. G. Jones, M. K. Chung, Y. Hassan, C. K. Nithianandan, and A. T. C. Tung, Phys. Fluids A **1**, 992 (1989).

[45] A. N. Beris and R. Sureshkumar, Chem. Eng. Sci. **51**, 1451 (1996).

[46] R. Sureshkumar, in *Flow Instabilities and Turbulence in Viscoelastic Fluids* (Lorentz Center Workshop, Leiden, 2010).

[47] P. Chakraborty, S. Balachandar, and R. J. Adrian, J. Fluid Mech. **535**, 189 (2005).

[48] M. D. Warholic, H. Massah, and T. J. Hanratty, Exp. Fluids **27**, 461 (1999).

[49] P. S. Virk, AIChE J. **21**, 625 (1975).